

Analog quantum simulation of chemical dynamics

Ryan J. MacDonell,^{1,4} Claire E. Dickerson,^{1,2,3,4} Clare J.T. Birch,^{1,4} Alok Kumar,⁵
 Claire L. Edmunds,^{2,3,4} Michael J. Biercuk,^{2,3,4} Cornelius Hempel,^{2,3,4} and Ivan Kassal^{1,4,*}

¹*School of Chemistry, University of Sydney, NSW 2006, Australia*

²*School of Physics, University of Sydney, NSW 2006, Australia*

³*ARC Centre of Excellence for Engineered Quantum Systems, University of Sydney, NSW 2006, Australia*

⁴*University of Sydney Nano Institute, University of Sydney, NSW 2006, Australia*

⁵*Department of Chemistry, Indian Institute of Technology Bombay, Mumbai, 400076, India*

Ultrafast chemical reactions are difficult to simulate because they involve entangled, many-body wavefunctions whose computational complexity grows rapidly with molecular size. In photochemistry, the breakdown of the Born-Oppenheimer approximation further complicates the problem by entangling nuclear and electronic degrees of freedom. Here, we show that analog quantum simulators can efficiently simulate molecular dynamics using commonly available bosonic modes to represent molecular vibrations. Our approach can be implemented in any device with a qudit controllably coupled to bosonic oscillators and with quantum hardware resources that scale linearly with molecular size, and with more than a ten-fold resource savings compared to digital quantum simulation algorithms. Advantages of our approach include a time resolution orders of magnitude better than ultrafast spectroscopy, the ability to simulate large molecules with limited hardware using a Suzuki-Trotter expansion, and the ability to implement realistic system-bath interactions with only one additional interaction per mode. Our approach can be implemented with current technology; e.g., the conical intersection in pyrazine can be simulated using a single trapped ion. Therefore, we expect our method will enable classically intractable chemical dynamics simulations in the near term.

Computational chemistry aims to predict energies, structures, reactivity, and other properties of molecules. Although molecular dynamics is, in principle, best simulated with a fully quantum-mechanical treatment of coupled electrons and nuclei, the computational cost of this approach scales exponentially with molecular size, making it intractable for most chemical systems. The cornerstone of the vast majority of quantum-chemistry methods is the Born-Oppenheimer (adiabatic) approximation, which neglects the coupling between electronic and nuclear degrees of freedom [1]. This approximation fails in regions of strong non-adiabatic coupling, particularly near degeneracies between electronic states, known as conical intersections [1]. Non-adiabatic couplings are essential to photochemistry, where conical intersections act as funnels from one electronic state to another on ultrafast timescales (those comparable to nuclear vibrational periods, fs-ps) [1, 2]. State-of-the-art algorithms, such as multiconfigurational time-dependent Hartree (MCTDH) [3, 4], can significantly reduce the simulation cost using a careful choice of basis-set contractions optimized for each system, enabling simulations of particular systems with tens to hundreds of modes [5–7]. Nevertheless, the optimal form of the MCTDH wavefunction cannot be predicted a priori, and the method—like all fully quantum-mechanical treatments of chemical dynamics—has an exponential worst-case scaling with system size.

Quantum computing promises to alleviate the steep computational cost of simulating quantum systems by representing the problem on a controllable quantum system [8]. Most research in chemical applications of quantum computing has focused on time-independent observables [9–14], in an effort to reduce the cost of electronic-structure methods. Such quantum methods involve the optimization of trial wavefunctions and mapping observables onto registers of qubits. Early work showed that molecular properties could be predicted with linearly many qubits and polynomially many

quantum gates as a function of molecule size [9, 10]. Due to limitations in qubit count and coherence times of current quantum computers, many recent methods use hybrid approaches, such as the variational quantum eigensolver, to divide the calculation into classical and quantum tasks [11–14]. By contrast, few quantum algorithms focus on the simulation of molecular dynamics. Proposed methods include the simulation of electronic [12] and vibrational [15] dynamics and the coupling between them [16, 17]. Although each of these methods scales polynomially with system size, their qubit requirements restrict them to small model systems.

Analog quantum simulators provide an alternative approach to quantum simulation by mapping a desired Hamiltonian onto a purpose-built quantum system. Quantum advantage has been demonstrated for classically-intractable simulations of Ising models [18, 19]. Analog simulators have been applied to several chemical problems: the simulation of vibrational dynamics [20] and Franck-Condon vibronic spectra [21, 22], electron transfer [23], and the electronic degrees of freedom of a molecule in a grid-based adiabatic picture [24].

Here, we show that analog quantum simulators can efficiently simulate non-adiabatic chemical dynamics. Our approach can be implemented using any quantum system containing a qudit with controllable couplings to a set of bosonic modes, a device we call a mixed qudit-boson (MQB) simulator. We achieve linear scaling in molecular size by mapping a molecule with d electronic states and N vibrational modes onto an MQB with a d -level qudit and N bosonic modes. Using bosonic degrees of freedom gives MQBs a ten-fold (or more) advantage over digital quantum simulations, which require many qubits to accurately represent a single harmonic oscillator. We analyze the non-adiabatic dynamics of pyrazine as an example, showing it can be simulated using a single trapped-ion MQB, and we detail how to extend the procedure to large systems using a Trotterization scheme and to open systems using laser cooling.

Hamiltonian mapping. Our approach uses vibronic coupling (VC) Hamiltonians, which are widely used to model chemical dynamics. They express molecular electronic matrix elements as analytical functions of the nuclear coordinates, often as a power series [1],

$$\hat{H} = \frac{1}{2} \sum_j \omega_j (\hat{Q}_j^2 + \hat{P}_j^2) + \sum_{n,m} \hat{C}_{n,m} |n\rangle \langle m|, \quad (1)$$

$$\hat{C}_{n,m} = c_0^{(n,m)} + \sum_j c_j^{(n,m)} \hat{Q}_j + \sum_{j,k} c_{j,k}^{(n,m)} \hat{Q}_j \hat{Q}_k + \dots, \quad (2)$$

where $|n\rangle$ is the n th electronic state, $\hat{Q}_j = (\mu_j \omega_j)^{1/2} \hat{q}_j$ and $\hat{P}_j = (\mu_j \omega_j)^{-1/2} \hat{p}_j$ are the dimensionless position and momentum of mode j (which has reduced mass μ_j , frequency ω_j , position \hat{q}_j , and momentum \hat{p}_j). We set $\hbar = 1$ throughout. The coefficients $c_0^{(n,m)}$, $c_j^{(n,m)}$, etc. are the (real) expansion coefficients of the nuclear potential energy about the reference geometry, typically the minimum of the ground electronic state. While adiabatic potential energy surfaces obtained from electronic structure methods are ill-behaved, with features such as conical intersections and singular kinetic-energy couplings, they can be transformed to the diabatic surfaces and couplings of VC Hamiltonians given by Eq. 2 (Fig. 1). For most applications, linear vibronic coupling (LVC) or quadratic vibronic coupling (QVC) models accurately represent photochemical observables [1, 25]. Note, however, that the expansion order has no effect on the classical memory required to store the wavefunction.

The similarity of VC and MQB Hamiltonians is seen if an LVC model is expressed in the interaction picture,

$$\hat{H}_I^{(1)} = \sum_{n \leq m} \sum_{j=1}^d c_j^{(n,m)} (|n\rangle \langle m| + \text{h.c.}) (\hat{a}_j^\dagger e^{i\omega_j t} + \text{h.c.}), \quad (3)$$

where \hat{a}_j^\dagger and \hat{a}_j are the bosonic creation and annihilation operators, corresponding to $\hat{Q}_j = (\hat{a}_j^\dagger + \hat{a}_j)/\sqrt{2}$. $\hat{H}_I^{(1)}$ is a generalized Jaynes-Cummings Hamiltonian describing the coupling of a d -level system to N bosonic modes. It is the same interaction that is used for digital quantum computation with existing architectures, including ion traps and cQED. Typically, ion-trap quantum computers encode qubits in the electronic states of the ions, and lasers are used to entangle them by coupling them through the trap vibrations [26–28]. Likewise, cQED uses microwave cavities coupled to superconducting qubits to implement multi-qubit gates [29]. In both cases, the Hamiltonian for the interaction of a single qubit with the bosonic modes takes the form of Eq. 3, meaning that the terms of an LVC Hamiltonian can be implemented with well-developed light-matter interactions. The MQB approach can also be extended to higher-order expansions; the second-order terms of a QVC Hamiltonian, in the interaction picture, become

$$\hat{H}_I^{(2)} = \sum_{n \leq m} \sum_{j \leq k} c_{j,k}^{(n,m)} (|n\rangle \langle m| + \text{h.c.}) \times (\hat{a}_j^\dagger \hat{a}_k e^{i(\omega_j - \omega_k)t} + \text{h.c.}). \quad (4)$$

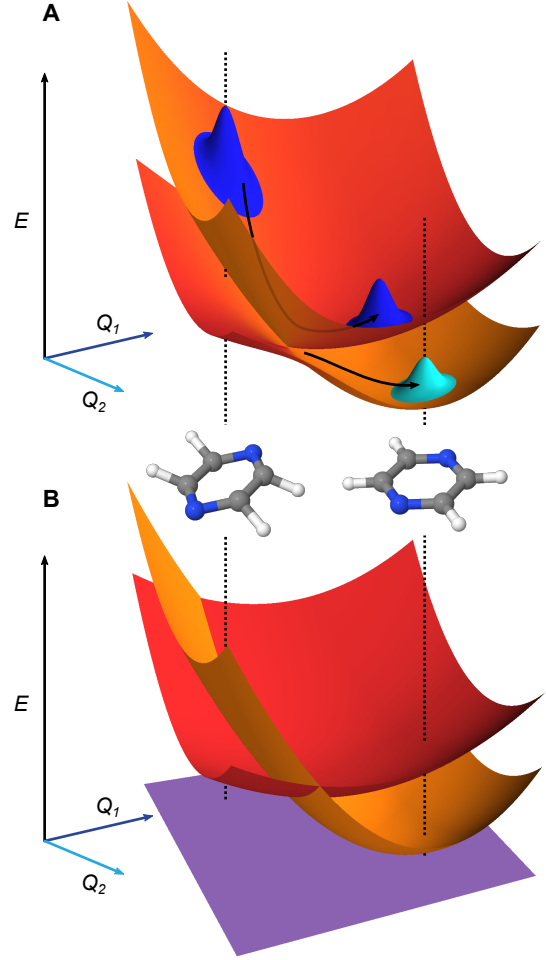


Figure 1. Representations of molecular potential-energy surfaces and their link to chemical dynamics. (A) Adiabatic surfaces correspond to the eigenvalues of the Born-Oppenheimer Hamiltonian at all nuclear displacements. The upper and lower surfaces shown correspond to higher- and lower-energy electronic states. Two inset molecules illustrate the different molecular geometries at two different sets of nuclear coordinates Q_1 and Q_2 . An initial wavepacket (blue, top left) can slide down the upper surface and, upon reaching the conical intersection (the cusp where the two surfaces are degenerate) it can split into two entangled branches (blue and cyan), one on each electronic surface. (B) Diabatic surfaces (red, orange) of a vibronic-coupling Hamiltonian (Eq. 1) formed from the adiabatic surfaces in A. The diabatic surfaces are analytic, avoiding numerical divergences near conical intersections. The couplings between the diabatic surfaces are not shown.

Both the dispersive ($j = k$) and mode-mixing ($j \neq k$) terms have been demonstrated experimentally in trapped ions [30, 31] and cQED [32, 33].

Overall, the numbers of qudit states and bosonic modes required for the MQB mapping scale linearly with the corresponding numbers of molecular degrees of freedom, a significant improvement over the exponential classical scaling of fully quantum-mechanical chemical dynamics methods. Fig. 2 shows that even optimised classical methods such as MCTDH are limited to tens of modes for many systems, meaning that even small MQBs could achieve quantum advantage. Fig. 2 also

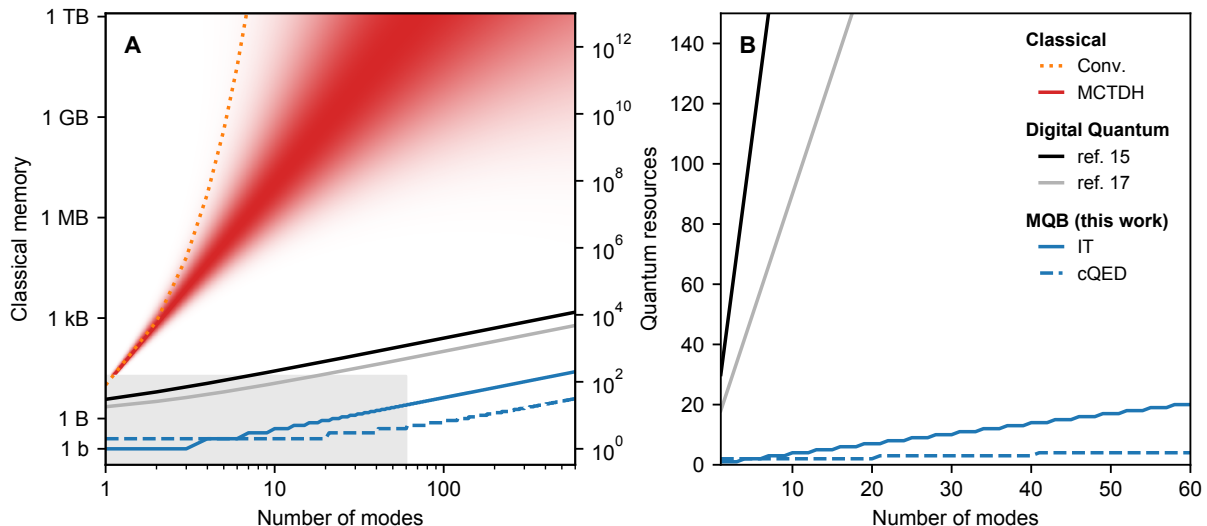


Figure 2. Resource (space) scaling of different methods for simulating vibronic dynamics. (A) Classical memory required for conventional (Conv.) and MCTDH approaches in bits (b) and bytes (B = 8b), and quantum hardware resources for digital and MQB approaches. For MCTDH, an approximate range is shown, because the performance of the method depends on the Hamiltonian and cannot be accurately predicted a priori. The quantum resources are qubits (for digital algorithms, assuming 8 qubits per simulated mode), ions (for ion-trap MQB, assuming 3 vibrations per ion), and microwave resonators (for cQED MQB, assuming 20 modes per resonator). (B) Linear-scale comparison of quantum approaches (range as the grey box in A).

shows that the MQB approach can simulate chemical dynamics with an improvement in quantum hardware requirements of over an order of magnitude compared to digital approaches [16, 17]. Its advantage is due to the natural mapping between molecular vibrations and MQB bosonic modes, which obviates the need, present on digital computers, to represent the large bosonic Hilbert space using qubits. The precise quantum requirements depend on the nature of the MQB simulator: if trapped ions are used, each ion produces three vibrational modes, while in circuit quantum electrodynamics (cQED), each resonator could yield dozens of microwave modes [34, 35]. The cost of the simulation can also be measured in the total number of interaction terms required, which scales as $N^k d(d+1)/2$ for an order- k expansion of Eq. 2. The vast majority of VC Hamiltonians are LVC models, which scale linearly with the number of vibrational modes, or QVC models, which scale quadratically [1]. The number of vibrations is a measure of the size of the molecule because it equals $N = 3N_n - 6$ in a molecule with N_n atoms. Furthermore, the simulation can sometimes be simplified by excluding certain modes or interactions that do not participate in the dynamics, either exactly (due to symmetry) or approximately (due to weak coupling).

Analog MQB simulation. An MQB simulation of molecular dynamics comprises three steps: initialization, evolution, and measurement.

Many initial states can readily be prepared on an MQB simulator using established techniques. In particular, in most photochemical studies, the Franck-Condon principle implies that photoexcitation only promotes the electronic degree of freedom to an excited state, leaving the vibrations unchanged [1]. On the MQB simulator, this corresponds to a change of the qudit state with no change to the bosonic state. In more general cases, superpositions of simulator qudit states could be prepared

to simulate molecules with nearly degenerate electronic states or undergoing broadband excitation. Sometimes, it is convenient to work in displaced nuclear coordinates, in which case the initial state must be displaced as well, as discussed in Appendix B.

Simulating the time evolution involves implementing qudit-boson interactions according to Eqs. 3–4 to mimic the VC Hamiltonian for the duration of the evolution. Given the correct light-matter interactions, the MQB simulator evolves in real time with the same dynamics as the VC model, except that the Hamiltonian can be arbitrarily scaled so that the evolution occurs on the natural timescale of the MQB simulator. The scaling freedom is a major advantage for the simulation: whereas molecular vibronic frequencies are typically 10-100 THz, MQB simulators operate at frequencies that are many orders of magnitude less (e.g., kHz for trapped ions and GHz for cQED). The dynamics on the simulator thus occur in extreme slow motion relative to the simulated molecule, giving the simulator much greater time resolution than ultrafast molecular spectroscopy.

Finally, after evolution for the desired amount of time, the MQB simulator can be probed to measure observables. Most chemically important observables do not require knowledge of the full wavefunction (which would require exponentially scaling full state tomography), and are instead easily measurable properties of the qudits or the bosons, such as the electronic-state populations or nuclear positions and momenta. Most MQB architectures have established methods for measuring qudit states; boson observables can also be measured, often by first mapping them onto the qudits [22, 36]. Due to the statistical nature of quantum measurement, observables must be averaged over many experiments, while repeating the experiment for different simulation times would yield temporal information. Importantly, the results at any simulation time are independent of the measure-

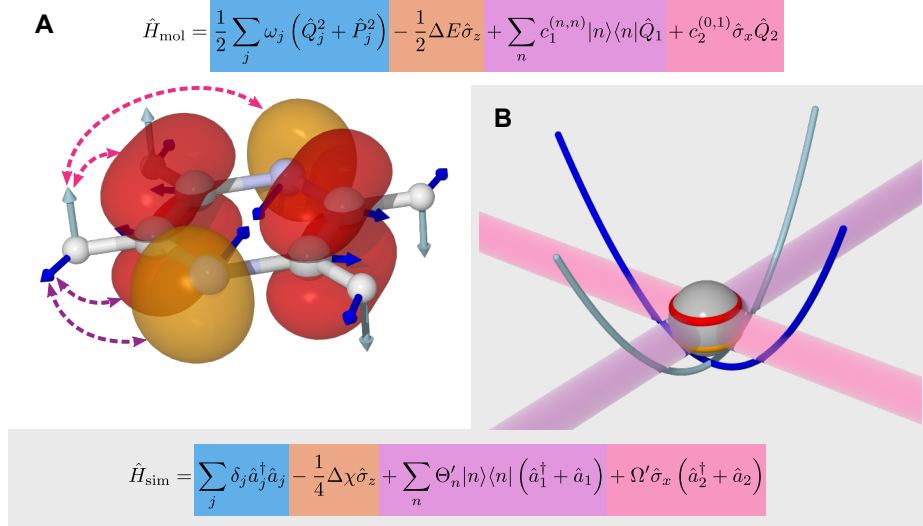


Figure 3. Example of the mapping between the degrees of freedom of a molecule (pyrazine, Eq. 5) and an MQB simulator (one trapped-ion qubit, Eq. 7). **(A)** The degrees of freedom of the molecule: electronic, shown as red and orange electronic orbitals; vibrational, shown as cyan and blue atomic displacements; and their couplings shown in purple and magenta. **(B)** The corresponding degrees of freedom for the trapped ion: qubit states (red and orange levels); bosonic modes (cyan and blue potential curves); and laser-mediated interactions (purple and magenta).

ments from previous times and the time intervals at which the measurements are made.

Example: 2D LVC model of pyrazine. To demonstrate our approach, we consider the MQB simulation of a two-state, two-mode LVC model of pyrazine using a single trapped ion (Fig. 3). Pyrazine is a canonical model system for molecular dynamics because the conical intersection between its two excited electronic states, the optically bright $\pi\pi^*$ state and the dark $n\pi^*$ state, is well described with only two modes. The vibrations comprise a fully symmetric (tuning) mode and a symmetry-breaking (coupling) mode [25, 37]. The ground electronic state is energetically separated from and weakly coupled to the excited states, meaning it can be excluded from the dynamics simulation [25]. The 2D LVC Hamiltonian is

$$\hat{H}_{\text{mol}} = \frac{1}{2} \sum_{j=1}^2 \omega_j (\hat{Q}_j^2 + \hat{P}_j^2) - \frac{1}{2} \Delta E \hat{\sigma}_z + \sum_{n=0}^1 c_1^{(n,n)} |n\rangle \langle n| \hat{Q}_1 + c_2^{(0,1)} \hat{\sigma}_x \hat{Q}_2, \quad (5)$$

where $|0\rangle$ and $|1\rangle$ are the $n\pi^*$ and $\pi\pi^*$ states, modes 1 and 2 are the tuning and coupling modes, $\hat{\sigma}_z$ and $\hat{\sigma}_x$ are Pauli matrices, and ΔE is the electronic energy difference at the ground-state-minimum geometry [25]. The initial state of the simulation is in the ground vibrational state, with the electronic state promoted to the $\pi\pi^*$ state, i.e., $|1\rangle \otimes |v_1 = 0\rangle \otimes |v_2 = 0\rangle$ for vibrational eigenstates v_j .

In the absence of a laser field, the Hamiltonian of a single, two-level trapped ion is

$$\hat{H}_{\text{ion}} = \sum_{j=1}^2 \omega_j^{\text{ion}} \hat{a}_j^\dagger \hat{a}_j - \frac{1}{2} \omega_0 \hat{\sigma}_z, \quad (6)$$

where ω_0 is the frequency difference between qubit states and ω_j^{ion} is the trap frequency of mode j . The diagonal

and off-diagonal couplings of Eq. 5 can be generated, respectively, by Raman interactions with bichromatic laser fields having frequency differences $\omega_j^{\text{ion}} - \delta_j$ and $\omega_0 \pm (\omega_j^{\text{ion}} - \delta_j)$, where δ_j is a small detuning [28]. The resulting Hamiltonian can be expressed in a rotating frame (see Appendix A) in the time-independent form

$$\hat{H}_{\text{sim}} = \sum_{j=1}^2 \delta_j \hat{a}_j^\dagger \hat{a}_j - \frac{1}{4} \Delta \chi \hat{\sigma}_z + \sum_{n=0}^1 \Theta'_n |n\rangle \langle n| (\hat{a}_1^\dagger + \hat{a}_1) + \Omega' \hat{\sigma}_x (\hat{a}_2^\dagger + \hat{a}_2), \quad (7)$$

where $\Delta \chi$ is the energy difference between qubit states induced by a time-independent AC Stark shift, Θ'_n is related to the time-dependent AC Stark shift of state n and Ω' is related to the Rabi frequency of the internal states of the ion (details in Appendix A).

Overall, the molecular and simulator Hamiltonians \hat{H}_{mol} and \hat{H}_{sim} are in exactly the same form, with $\hat{Q}_j = (\hat{a}_j^\dagger + \hat{a}_j)/\sqrt{2}$ and $\hat{P}_j = i(\hat{a}_j^\dagger - \hat{a}_j)/\sqrt{2}$ (Fig. 3). Mapping the molecule onto the simulator thus involves selecting (up to a timescale rescaling) detunings δ_j to match the molecular vibrational frequencies ω_j , the time-independent Stark shift $\Delta \chi/2$ to match the molecular energy difference ΔE , and the time-dependent Stark shifts and Rabi frequencies, Θ'_n and Ω' , to match the coupling parameters $c_1^{(n,n)}$ and $c_2^{(0,1)}$.

The initialization, evolution, and measurement steps of a pyrazine simulation are illustrated in Fig. 4A–C. This simulation can be simplified by working in a displaced frame, which can transform the tuning term (third term in Eq. 7) to either $\sigma_z(\hat{a}_1^\dagger + \hat{a}_1)$ or $|1\rangle \langle 1| (\hat{a}_1^\dagger + \hat{a}_1)$, which are more easily implemented in trapped ions (details in Appendix B). To compensate for the frame displacement, Fig. 4A shows an initial wavefunction displacement.

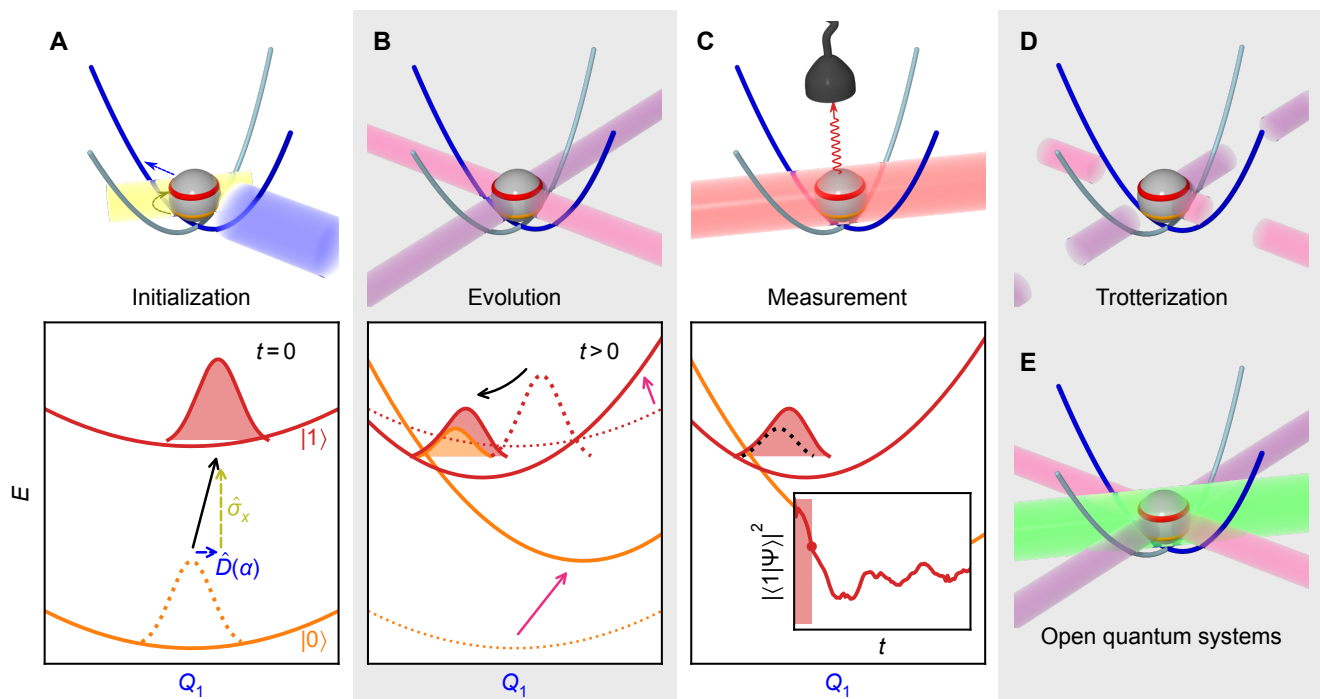


Figure 4. Illustrative molecular-dynamics simulation using an MQB simulator (trapped-ion qubit for concreteness). (A) The initial wavefunction is prepared by an excitation of the qudit state (yellow arrow/laser) and a displacement along the relevant mode(s) (blue arrow/laser). (B) The VC Hamiltonian is implemented through interactions with laser fields (purple and magenta, see Eq. 3), which are equivalent to displacements and couplings between potential energy surfaces. These interactions are maintained for the duration of the simulation. (C) After evolution by the effective Hamiltonian, observables of the wavefunction (inset: excited state population) are measured by a detector (e.g., fluorescence of the qubit state induced by the red laser). Multiple measurements are required to obtain expectation values, and the time dependence of observables is obtained by varying the time delay from initialization to measurement. (D) The evolution step can be discretized using a Suzuki-Trotter expansion into a series of short laser interactions, particularly for the treatment of many modes. (E) Open quantum systems can be simulated by adding sideband laser cooling (green) during the evolution step.

Extensions. So far, we assumed that all VC interactions can be implemented simultaneously on an MQB simulator. This may not be practical for simulations with many interaction terms, because it would require a separate light-matter interaction for each. Instead, the evolution of the wavefunction can be discretized with a Suzuki-Trotter expansion [38] by applying sets of terms in sequence for short times (Fig. 4D), allowing the same laser to implement multiple interactions. As in many analog simulations, the problem is complicated by the fact that the Hamiltonian of an MQB simulator is non-zero in the absence of interactions. In Appendix C, we detail how a Suzuki-Trotter expansion can nevertheless be implemented, taking the continuous simulator evolution into account. For the first-order Suzuki-Trotter expansion, the error scales with the square of the Trotter time step, Δt^2 . If a Suzuki-Trotter expansion is used, the simulation is no longer limited by the number of interactions that can be implemented simultaneously; instead, there is a trade-off between the simulation accuracy and the number of Trotter steps.

MQB devices also allow the simulation of open quantum systems—such as molecules in the condensed phase—with minimal overhead. In general, open-system simulation is even more computationally expensive on classical computers, as it involves the evolution of a density matrix rather than a state vector. Classical MCTDH simulation have been achieved with weak coupling to

baths, but increasing the number of bath modes quickly becomes intractable [3, 4]. Implementing dissipation on an MQB simulator would depend on the nature of the available environmental couplings. For example, analog simulations with trapped ions have demonstrated the ability to simulate electronic dissipation with optical pumping [39] and vibrational dissipation with sympathetic laser cooling [23]. In Appendix D, we extend the latter approach to simulate non-zero temperatures with at most one sideband-cooling interaction per vibrational mode, representing weak coupling of molecular vibrations to a harmonic oscillator bath. Our approach allows the system-bath coupling strength to be controlled by the laser intensity and the effective simulated temperature by the detuning of the cooling laser from the trap frequency (Fig. 4E). Thus, ion-trap MQB devices can simulate open chemical systems with existing techniques, at a cost that scales linearly with the number of modes coupled to the environment.

The one-to-one correspondence of molecular and simulator degrees of freedom gives MQB simulators a clear advantage in the simulation of non-adiabatic chemical dynamics over both classical and qubit-based schemes. For an increasing number of vibrational modes, our approach requires linearly scaling quantum hardware and polynomially many interaction terms, in either isolated or open molecular systems. For large systems, the number of simultaneous interactions can be significantly

reduced with a Suzuki-Trotter expansion, allowing the same driving fields to be reused. Scaling the frequencies of the VC Hamiltonian to the MQB simulator also offers a significant advantage in time resolution relative to ultrafast spectroscopy experiments. Many of the tools necessary for MQB simulation have been developed in the context of universal quantum computation and can be easily repurposed for analog simulation, making MQB simulators a promising platform for a clear quantum advantage in the simulation of chemical dynamics. Indeed, we expect that dynamical simulations such as these will more easily achieve quantum advantage than solving time-independent electronic-structure problems.

Acknowledgements

We acknowledge valuable discussion with Alistair Milne, Ramil Nigmatullin, Ting Rei Tan, and Joel Yuen-

Zhou. We were supported by a Westpac Scholars Trust Research Fellowship, by the Lockheed Martin Corporation, by the Australian Government's Defence Science and Technology Group, by the United States Office of Naval Research Global (N62909-20-1-2047), and by the University of Sydney Nano Institute Grand Challenge *Computational Materials Discovery*. We were supported by computational resources and assistance from the National Computational Infrastructure (NCI) and the University of Sydney's computing cluster Artemis.

* ivan.kassal@sydney.edu.au

- [1] W. Domcke, D. R. Yarkony, and H. Köppel, eds., *Conical Intersections: Electronic Structure, Dynamics & Spectroscopy*, Adv. Ser. Phys. Chem., Vol. 15 (World Scientific, Singapore, 2004).
- [2] L. S. Cederbaum, H. Köppel, and W. Domcke, *Int. J. Quantum Chem.* **20**, 251 (1981).
- [3] G. A. Worth, H.-D. Meyer, H. Köppel, L. S. Cederbaum, and I. Burghardt, *Int. Rev. Phys. Chem.* **27**, 569 (2008).
- [4] H. Wang, *J. Phys. Chem. A* **119**, 7951 (2015).
- [5] Q. Meng and H.-D. Meyer, *J. Chem. Phys.* **138**, 014313 (2013).
- [6] Y. Xie, J. Zheng, and Z. Lan, *J. Chem. Phys.* **142**, 084706 (2015).
- [7] J. Schulze, M. F. Shibl, M. J. Al-Marri, and O. Kühn, *J. Chem. Phys.* **144**, 185101 (2016).
- [8] M. A. Nielsen and I. L. Chuang, *Quantum Computation and Quantum Information* (Cambridge University Press, Cambridge, UK, 2000).
- [9] A. Aspuru-Guzik, A. D. Dutoi, P. J. Love, and M. Head-Gordon, *Science* **309**, 1704 (2005).
- [10] B. P. Lanyon, J. D. Whitfield, G. G. Gillett, M. E. Goggin, M. P. Almeida, I. Kassal, J. D. Biamonte, M. Mohseni, B. J. Powell, M. Barbieri, A. Aspuru-Guzik, and A. G. White, *Nat. Chem.* **2**, 106 (2010).
- [11] A. Peruzzo, J. McClean, P. Shadbolt, M.-H. Yung, X.-Q. Zhou, P. J. Love, A. Aspuru-Guzik, and J. L. O'Brien, *Nat. Commun.* **5**, 4213 (2014).
- [12] Y. Li and S. C. Benjamin, *Phys. Rev. X* **7**, 021050 (2017).
- [13] C. Hempel, C. Maier, J. Romero, J. McClean, T. Monz, H. Shen, P. Jurcevic, B. P. Lanyon, P. Love, R. Babbush, A. Aspuru-Guzik, R. Blatt, and C. F. Roos, *Phys. Rev. X* **8**, 031022 (2018).
- [14] F. Arute, K. Arya, R. Babbush, D. Bacon, J. C. Bardin, R. Barends, S. Boixo, M. Broughton, B. B. Buckley, D. A. Buell, B. Burkett, N. Bushnell, Y. Chen, Z. Chen, B. Chiaro, R. Collins, W. Courtney, S. Demura, A. Dunsworth, D. Eppens, E. Farhi, A. Fowler, B. Foxen, C. Gidney, M. Giustina, R. Graff, S. Habegger, M. P. Harrigan, A. Ho, S. Hong, T. Huang, W. J. Huggins, L. Ioffe, S. V. Isakov, E. Jeffrey, Z. Jiang, C. Jones, D. Kafri, K. Kechedzhi, J. Kelly, S. Kim, P. V. Klimov, A. Korotkov, F. Kostitsa, D. Landhuis, P. Laptev, M. Lindmark, E. Lucero, O. Martin, J. M. Martinis, J. R. McClean, M. McEwen, A. Megrant, X. Mi, M. Mohseni, W. Mruczkiewicz, J. Mutus, O. Naaman, M. Neeley, C. Neill, H. Neven, M. Y. Niu, T. E. O'Brien, E. Ostby, A. Petukhov, H. Putterman, C. Quintana, P. Roushan, N. C. Rubin, D. Sank, K. J. Satzinger, V. Smelyanskiy, D. Strain, K. J. Sung, M. Szalay, T. Y. Takeshita, A. Vainsencher, T. White, N. Wiebe, Z. J. Yao, P. Yeh, and A. Zalcman, *Science* **369**, 1084 (2020).
- [15] S. McArdle, A. Mayorov, X. Shan, S. Benjamin, and X. Yuan, *Chem. Sci.* **10**, 5725 (2019).
- [16] I. Kassal, S. P. Jordan, P. J. Love, M. Mohseni, and A. Aspuru-Guzik, *Proc. Natl. Acad. Sci.* **105**, 18681 (2008).
- [17] P. J. Ollitrault, G. Mazzola, and I. Tavernelli, arXiv (2020), 2006.09405.
- [18] J. W. Britton, B. C. Sawyer, A. C. Keith, C.-C. J. Wang, J. K. Freericks, H. Uys, M. J. Biercuk, and J. J. Bollinger, *Nature* **484**, 489 (2012).
- [19] J. Zhang, G. Pagano, P. W. Hess, A. Kyprianidis, P. Becker, H. Kaplan, A. V. Gorshkov, Z.-X. Gong, and C. Monroe, *Nature* **551**, 601 (2017).
- [20] C. Sparrow, E. Martín-López, N. Maraviglia, A. Neville, C. Harrold, J. Carolan, Y. N. Joglekar, T. Hashimoto, N. Matsuda, J. L. O'Brien, D. P. Tew, and A. Laing, *Nature* **557**, 660 (2018).
- [21] J. Huh, G. G. Guerreschi, B. Peropadre, J. R. McClean, and A. Aspuru-Guzik, *Nat. Photonics* **9**, 615 (2015).
- [22] C. S. Wang, J. C. Curtis, B. J. Lester, Y. Zhang, Y. Y. Gao, J. Freeze, V. S. Batista, P. H. Vaccaro, I. L. Chuang, L. Frunzio, L. Jiang, S. M. Girvin, and R. J. Schoelkopf, *Phys. Rev. X* **10**, 021060 (2020).
- [23] F. Schlawin, M. Gessner, A. Buchleitner, T. Schaetz, and S. S. Skourtis, arXiv (2020), 2004.02925.
- [24] J. Argüello-Luengo, A. González-Tudela, T. Shi, P. Zoller, and J. I. Cirac, *Nature* **574**, 215 (2019).
- [25] L. Seidner, G. Stock, A. L. Sobolewski, and W. Domcke, *J. Chem. Phys.* **96**, 5298 (1992).
- [26] K. Mølmer and A. Sørensen, *Phys. Rev. Lett.* **82**, 1835 (1999).
- [27] D. Leibfried, B. DeMarco, V. Meyer, D. Lucas, M. Barrett, J. Britton, W. M. Itano, B. Jelenković, C. Langer, T. Rosenband, and D. J. Wineland, *Nature* **422**, 412 (2003).

- [28] P. J. Lee, K.-A. Brickman, L. Deslauriers, P. C. Haljan, L.-M. Duan, and C. Monroe, *J. Opt. B: Quantum Semiclass. Opt.* **7**, S371 (2005).
- [29] A. Blais, R.-S. Huang, A. Wallraff, S. M. Girvin, and R. J. Schoelkopf, *Phys. Rev. A* **69**, 062320 (2004).
- [30] J. S. Pedernales, I. Lizuain, S. Felicetti, G. Romero, L. Lamata, and E. Solano, *Sci. Rep.* **5**, 15472 (2015).
- [31] K. Marshall and D. F. V. James, *Appl. Phys. B* **123**, 26 (2016).
- [32] A. Blais, S. M. Girvin, and W. D. Oliver, *Nat. Phys.* **16**, 247 (2020).
- [33] Y. Y. Gao, B. J. Lester, Y. Zhang, C. Wang, S. Rosenblum, L. Frunzio, L. Jiang, S. M. Girvin, and R. J. Schoelkopf, *Phys. Rev. X* **8**, 021073 (2018).
- [34] N. M. Sundaresan, Y. Liu, D. Sadri, L. J. Szöcs, D. L. Underwood, M. Malekakhlagh, H. E. Türeci, and A. A. Houck, *Phys. Rev. X* **5**, 021035 (2015).
- [35] A. J. Kollár, M. Fitzpatrick, and A. A. Houck, *Nature* **571**, 45 (2019).
- [36] R. Gerritsma, B. P. Lanyon, G. Kirchmair, F. Zähringer, C. Hempel, J. Casanova, J. J. García-Ripoll, E. Solano, R. Blatt, and C. F. Roos, *Phys. Rev. Lett.* **106**, 060503 (2011).
- [37] A. Kühl and W. Domcke, *J. Chem. Phys.* **116**, 263 (2002).
- [38] S. Lloyd, *Phys. Rev. Lett.* **75**, 346 (1995).
- [39] J. T. Barreiro, M. Müller, P. Schindler, D. Nigg, T. Monz, M. Chwalla, M. Hennrich, C. F. Roos, P. Zoller, and R. Blatt, *Nature* **470**, 486 (2011).
- [40] A. Sørensen and K. Mølmer, *Phys. Rev. Lett.* **82**, 1971 (1999).
- [41] C. Hempel, B. P. Lanyon, P. Jurcevic, R. Gerritsma, R. Blatt, and C. F. Roos, *Nature Photon.* **7**, 630 (2013).
- [42] K. Hosaka, S. A. Webster, A. Stannard, B. R. Walton, H. S. Margolis, and P. Gill, *Phys. Rev. A* **79**, 033403 (2009).
- [43] C. L. Edmunds, T. R. Tan, A. Milne, A. Singh, M. Biercuk, and C. Hempel, in preparation (2020).
- [44] B. Vlastakis, G. Kirchmair, Z. Leghtas, S. E. Nigg, L. Frunzio, S. M. Girvin, M. Mirrahimi, M. H. Devoret, and R. J. Schoelkopf, *Science* **342**, 607 (2013).
- [45] V. Gorini, A. Kossakowski, and E. C. G. Sudarshan, *J. Math. Phys.* **17**, 821 (1976).
- [46] G. Lindblad, *Commun. Math. Phys.* **48**, 119 (1976).
- [47] S. Stenholm, *Rev. Mod. Phys.* **58**, 699 (1986).
- [48] F. Diedrich, J. C. Bergquist, W. M. Itano, and D. J. Wineland, *Phys. Rev. Lett.* **62**, 403 (1989).
- [49] R. Lechner, C. Maier, C. Hempel, P. Jurcevic, B. P. Lanyon, T. Monz, M. Brownnutt, R. Blatt, and C. F. Roos, *Phys. Rev. A* **93**, 053401 (2016).
- [50] C. R. Harris, K. J. Millman, S. J. van der Walt, R. Gommers, P. Virtanen, D. Cournapeau, E. Wieser, J. Taylor, S. Berg, N. J. Smith, R. Kern, M. Picus, S. Hoyer, M. H. van Kerkwijk, M. Brett, A. Haldane, J. F. del Río, M. Wiebe, P. Peterson, P. Gérard-Marchant, K. Sheppard, T. Reddy, W. Weckesser, H. Abbasi, C. Gohlke, and T. E. Oliphant, *Nature* **585**, 357 (2020).
- [51] P. Virtanen, R. Gommers, T. E. Oliphant, M. Haberland, T. Reddy, D. Cournapeau, E. Burovski, P. Peterson, W. Weckesser, J. Bright, S. J. van der Walt, M. Brett, J. Wilson, K. J. Millman, N. Mayorov, A. R. J. Nelson, E. Jones, R. Kern, E. Larson, C. J. Carey, I. Polat, Y. Feng, E. W. Moore, J. VanderPlas, D. Laxalde, J. Perktold, R. Cimrman, I. Henriksen, E. A. Quintero, C. R. Harris, A. M. Archibald, A. H. Ribeiro, F. Pedregosa, P. van Mulbregt, and SciPy 1.0 Contributors, *Nat. Methods* **17**, 261 (2020).
- [52] J. R. Johansson, P. D. Nation, and F. Nori, *Comp. Phys. Comm.* **184**, 1234 (2013).

APPENDICES

A. Light-matter interactions in trapped-ion simulators

Here, we follow ref. 28 to derive the light-matter interactions required to map an LVC Hamiltonian onto an ion-trap Hamiltonian.

Tuning terms in the LVC Hamiltonian can be generated using two non-copropagating lasers, which can induce Raman transitions that couple the internal states of an N -level trapped ion with its vibrational mode j (frequency ω_j^{ion}). If the frequency between the two lasers is $\omega_j^{\text{ion}} - \delta_j$, the resulting interaction-picture Hamiltonian becomes

$$\hat{H}_I^t = \frac{1}{2} \eta_j D_j' \sum_n \Theta_{n,j} |n\rangle \langle n| (\hat{a}_j^\dagger e^{i(\delta_j t - \phi)} + \text{h.c.}), \quad (\text{A1})$$

where η_j is the Lamb-Dicke parameter, D_j' is the Debye-Waller factor, and $\Theta_{n,j}$ is the time-dependent AC Stark shift of state n . The interaction of Eq. A1 is well established; in particular, the two-qubit generalisation is widely used to implement the phase gate $\hat{\sigma}_z \otimes \hat{\sigma}_z$ [27]. This form of the Hamiltonian assumes that the intermediate state $|e\rangle$ can be adiabatically eliminated, i.e., that the global detuning Δ of ω_α and ω_β from $|e\rangle$ is much larger than the linewidth γ_e of $|e\rangle$, and that the detuning δ_j is small relative to the ion trap frequency ω_j^{ion} . The laser field also causes a time-independent AC Stark shift for each state, $\chi^{(n)}$, which modulates the internal state energies and can be experimentally tuned by Δ [27]. Without loss of generality, the phase ϕ can be dropped as it corresponds to an arbitrary initial phase-space angle.

Coupling terms in the LVC Hamiltonian can be generated if, instead, the difference between the laser frequencies is $\Delta E_{n,m}^{\text{ion}} \pm (\omega_k^{\text{ion}} - \delta_k)$, where $\Delta E_{n,m}^{\text{ion}}$ is the energy difference between internal states n and m , and the plus or minus determining whether the interaction corresponds to a blue- or red-sideband transition. The sum of red and blue sideband terms gives a Hamiltonian of the form

$$\hat{H}_I^c = \frac{1}{2} \eta_k D_k' \Omega_{n,m,k} (|n\rangle \langle m| e^{i\phi_S} + \text{h.c.}) \times (\hat{a}_k^\dagger e^{i(\delta_k t - \phi_M)} + \text{h.c.}), \quad (\text{A2})$$

where $\Omega_{n,m,k}$ is the base Rabi frequency of the internal states, ϕ_S is the spin-phase of the ion resulting from the sum of the two transitions, and ϕ_M is the phase difference between the red and blue sidebands. As with the interaction above, this interaction is widely used, especially to generate the Mølmer-Sørensen entangling gate [26, 40]. Setting $\phi_S = 0$ results in an interstate coupling in the same form as in the LVC Hamiltonian. As with ϕ before, the phase ϕ_M can be dropped.

The total interaction Hamiltonian is obtained by adding an instance of Eq. A1 for each tuning mode and an instance of Eq. A2 for each coupling mode. Once the time-independent AC Stark shifts χ_n are also included,

the total Hamiltonian becomes

$$\begin{aligned}\hat{H}_I = & \sum_{j \in \mathbf{t}} \sum_n \Theta'_{n,j} |n\rangle \langle n| (\hat{a}_j^\dagger e^{i\delta_j t} + \text{h.c.}) \\ & + \sum_{k \in \mathbf{c}} \sum_{m < n} \Omega'_{n,m,k} (|n\rangle \langle m| + \text{h.c.}) \\ & \times (\hat{a}_k^\dagger e^{i\delta_k t} + \text{h.c.}) + \frac{1}{2} \sum_n \chi_n |n\rangle \langle n|, \quad (\text{A3})\end{aligned}$$

where $\Theta'_{n,j} = \eta_j D'_j \Theta_{n,j}/2$, $\Omega'_{n,m,k} = \eta_k D'_k \Omega_{n,m,k}/2$ and the sets \mathbf{t} and \mathbf{c} are indices of tuning and coupling modes, respectively. This Hamiltonian can be transformed into a rotating frame to give

$$\begin{aligned}\hat{H} = & \sum_j \delta_j \hat{a}_j^\dagger \hat{a}_j + \frac{1}{2} \sum_n \chi_n |n\rangle \langle n| \\ & + \sum_{j \in \mathbf{t}} \sum_n \Theta'_{n,j} |n\rangle \langle n| (\hat{a}_j^\dagger + \hat{a}_j) \\ & + \sum_{k \in \mathbf{c}} \sum_{m < n} \Omega'_{n,m,k} (|n\rangle \langle m| + |m\rangle \langle n|) (\hat{a}_k^\dagger + \hat{a}_k).\end{aligned} \quad (\text{A4})$$

The results above are general for any number of internal states and any number of vibrational modes. Although a single ion has only three vibrational modes, additional modes can be obtained by adding ancillary, optically inactive ions into the trap. The ancillary ions can be made optically inactive in multiple ways, including the use of different isotopes [41] or by pumping them into long-lived shelved states [42, 43].

For a two-state system with two modes, Eq. A4 simplifies to Eq. 7 of the main text.

B. Displaced vibronic-coupling Hamiltonians

For experimental implementation of VC Hamiltonian simulations, it may be convenient to transform the elements of the Hamiltonian into a different form. In particular, the interstate coupling factors of the form $\sum_{n \leq m} c_j^{(n,m)} (|n\rangle \langle m| + \text{h.c.})$ can be replaced with more easily implemented operators, such as $\hat{\sigma}_x$ or $\hat{\sigma}_z$.

One way to do this is by a coherent displacement of the Hamiltonian along a single mode. This corresponds to the action of a displacement operator, $\hat{D}_k(\beta) = \exp(-i\beta \hat{P}_k)$ for mode k and real β , where

$$\hat{D}_k(\beta) \hat{Q}_k \hat{D}_k^\dagger(\beta) = \hat{Q}_k - \beta \quad (\text{B1})$$

is a change in position by β along mode k . For a general VC Hamiltonian (Eq. 1), the displacement gives

$$\begin{aligned}\hat{H}' = & \hat{D}_k \hat{H} \hat{D}_k^\dagger = \hat{H} - \omega_k \beta \hat{Q}_k + \frac{1}{2} \omega_k \beta^2 \\ & - \sum_{n,m} \left(\beta c_k^{(n,m)} - \beta^2 c_{k,k}^{(n,m)} \right. \\ & \left. + 2\beta \sum_j c_{k,j}^{(n,m)} \hat{Q}_j + \dots \right) |n\rangle \langle m|. \quad (\text{B2})\end{aligned}$$

Dropping the constant term $\omega_k \beta^2/2$ and truncating to linear terms ($c_{k,j,\dots}^{(n,m)} = 0$) yields the displaced LVC Hamiltonian,

$$\hat{H}'_{\text{LVC}} = \hat{H}_{\text{LVC}} - \sum_{n,m} \left(\beta c_k^{(n,m)} + \beta \omega_k \delta_{n,m} \hat{Q}_k \right) |n\rangle \langle m|, \quad (\text{B3})$$

where $\delta_{n,m}$ is a Kronecker delta, meaning only the diagonal elements ($n = m$) of first-order terms are affected by displacement.

In the two-state case ($n, m \in \{0, 1\}$), the electronic components of the LVC Hamiltonian can be expressed in terms of Pauli operators to yield

$$\begin{aligned}\hat{H}_{\text{LVC}} = & \frac{1}{2} \sum_j \omega_j \left(\hat{Q}_j^2 + \hat{P}_j^2 \right) - \frac{1}{2} \Delta E \hat{\sigma}_z + W_0 \hat{\sigma}_x \\ & + \sum_j \left(\bar{\kappa}_j - \frac{1}{2} \Delta \kappa_j \hat{\sigma}_z + \lambda_j \hat{\sigma}_x \right) \hat{Q}_j, \quad (\text{B4})\end{aligned}$$

where $\Delta E = c_0^{(1,1)} - c_0^{(0,0)}$, $W_0 = c_0^{(0,1)}$, $\bar{\kappa}_j = (c_j^{(1,1)} + c_j^{(0,0)})/2$, $\Delta \kappa_j = c_j^{(1,1)} - c_j^{(0,0)}$ and $\lambda_j = c_j^{(0,1)}$. After displacement along mode k ,

$$\hat{H}'_{\text{LVC}} = \hat{H}_{\text{LVC}} - \beta \left(-\frac{1}{2} \Delta \kappa_k \hat{\sigma}_z + \lambda_k \hat{\sigma}_x + \omega_k \hat{Q}_k \right), \quad (\text{B5})$$

where the constant energy $\beta \bar{\kappa}_k$ is excluded as it only contributes a global phase. This is equivalent to making the replacements $\Delta E \rightarrow \Delta E - \beta \Delta \kappa_k$, $W_0 \rightarrow W_0 - \beta \lambda_k$ and $\bar{\kappa}_k \rightarrow \bar{\kappa}_k - \beta \omega_k$, which could be used to simplify the Hamiltonian. For example, choosing $\beta = \bar{\kappa}_k/\omega_k$ would remove the $\mathbb{1} \otimes \hat{Q}_k$ term from Eq. B4.

The dynamics simulated with the displaced VC Hamiltonian is exactly equivalent (i.e., produces the same observables) to that of the original model as long as the initial wavefunction is displaced by an equal amount, which is achievable for common bosonic simulators [41, 44].

C. Analog Trotterization

When all terms of a Hamiltonian cannot be implemented simultaneously, time evolution of the simulator can be split into components using a Suzuki-Trotter expansion [38]. On digital simulators, Trotterization is routine because it is easy for particular Trotter steps to act on certain degrees of freedom while leaving the others unchanged. On analog simulators, however, Trotterization is complicated by the fact that a part of the Hamiltonian cannot be turned off, and continues to evolve continuously during each interaction term. For example, in trapped ions, all vibrational degrees of freedom continue to oscillate in the trapping potential even if interaction lasers are only perturbing some of them.

Here, we offer two approaches to analog Trotterization. We assume that the base Hamiltonian \hat{H}_0 cannot be turned off, while interaction Hamiltonians \hat{H}_k , for $1 \leq k \leq M$, can be turned on and off on demand.

The first, *rescaling*, approach relies on the fact that, in an analog simulation, the total Hamiltonian can be scaled by a constant factor, changing only the speed of the simulation. In addition, the individual terms themselves can be rescaled, as long as the total Hamiltonian is proportional to the Hamiltonian to be simulated. In particular, we can re-express the full Hamiltonian as

$$\hat{H} = \hat{H}_0 + \sum_{k=1}^M \hat{H}_k = \sum_{k=1}^M (\hat{H}_0/M + \hat{H}_k). \quad (C1)$$

In that case, the first-order Suzuki-Trotter evolution (for a short timestep Δt) is

$$U_1(\Delta t) = \prod_{k=1}^M \exp(-i(\hat{H}_0/M + \hat{H}_k)\Delta t). \quad (C2)$$

Essentially, the evolution by the base Hamiltonian is slowed down relative to the interaction terms to compensate for the continuous evolution under \hat{H}_0 while each of the \hat{H}_k is implemented in turn. Of course, higher-order Suzuki-Trotter expansions can be used to reduce the Trotterization error.

The second, *rewinding*, approach treats the base Hamiltonian and interaction terms on the same timescale (i.e., without rescaling), opting instead to reverse the excessive evolution under the base Hamiltonian. This approach assumes that time evolution under $-\hat{H}_0$ can be implemented between Trotter steps. At first order, this scheme is given by

$$\hat{U}_1(\Delta t) = \exp(-i\hat{H}_0\Delta t) \times \prod_{k=1}^M \left(\exp(i\hat{H}_0\Delta t) \exp(-i(\hat{H}_0 + \hat{H}_k)\Delta t) \right), \quad (C3)$$

i.e., by correcting the evolution by $\exp(i\hat{H}_0\Delta t)$ after each Trotter step, which can be thought of as implementing another unitary of the form $\exp(-i(-2\hat{H}_0)\Delta t)$ while the base Hamiltonian is always on.

The two approaches have similar performance, as can be seen in the example of a two-mode system (e.g., the LVC Hamiltonian of pyrazine), where the time evolution operators for a single timestep become

$$\hat{U}_1^{\text{res.}}(\Delta t) = \exp(-i(\hat{H}_0/2 + \hat{H}_2)\Delta t) \times \exp(-i(\hat{H}_0/2 + \hat{H}_1)\Delta t), \quad (C4)$$

$$\hat{U}_1^{\text{rew.}}(\Delta t) = \exp(-i(\hat{H}_0 + \hat{H}_2)\Delta t) \exp(i\hat{H}_0\Delta t) \times \exp(-i(\hat{H}_0 + \hat{H}_1)\Delta t), \quad (C5)$$

where the superscripts res. and rew. denote rescaling and rewinding approaches, respectively. The effect of Trotterization is shown in Fig. 5: as expected, increasing the Trotter step Δt increase the error in the electronic population (Fig. 5A). The fidelities (Fig. 5B) show larger errors; however, fidelities of both rescaling and rewinding approaches are nearly identical, indicating that either may be used for simulations.

The difference between the two approaches arises in the limit of many interaction terms, where one approach

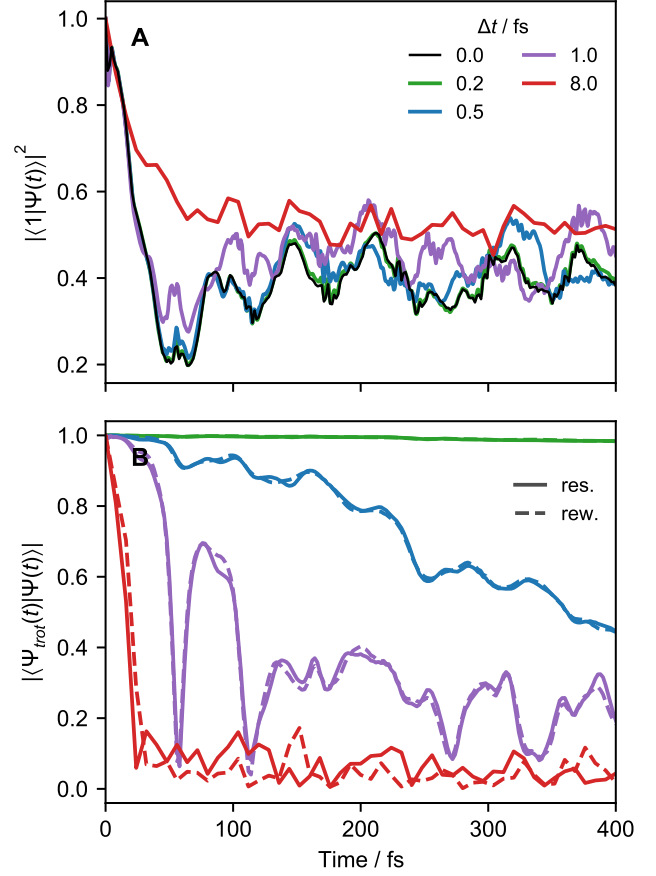


Figure 5. Evaluation of Trotterization approaches using the pyrazine LVC Hamiltonian. (A) Electronic populations as a function of time with different Trotter steps Δt . The rescaling approach was used in all cases. (B) Comparison of the fidelities of the rescaling and rewinding approaches. The fidelity measures the overlap of the Trotterized wavefunction, $|\Psi_{\text{trot}}(t)\rangle$, with the exact wavefunction, $|\Psi(t)\rangle$ ($\Delta t = 0$). Results for rescaling are given by solid lines and for rewinding by dashed lines, showing no significant difference.

may be preferred over another depending on experimental limitations. The strength of the rescaling approach is that it requires fewer operations to be implemented on the simulator, while the strength of the rewinding approach is that it ensures that all components evolve at the same speed.

D. Open-quantum system simulation on trapped-ion simulators

Finding the dynamics of an open quantum system involves solving a quantum master equation for the reduced density operator $\hat{\rho}$ of a system interacting with a bath. In the limit of weak system-bath coupling, the system evolution is often assumed to be in Lindblad form [45, 46]

$$\begin{aligned} \partial \hat{\rho} / \partial t &= -i[\hat{H}, \hat{\rho}] + \sum_j \left(\hat{L}_j \hat{\rho} \hat{L}_j^\dagger - \frac{1}{2} \{ \hat{L}_j^\dagger \hat{L}_j, \hat{\rho} \} \right) \\ &= -i[\hat{H}, \hat{\rho}] + \sum_j \mathcal{D}[\hat{L}_j] \hat{\rho}, \end{aligned} \quad (D1)$$

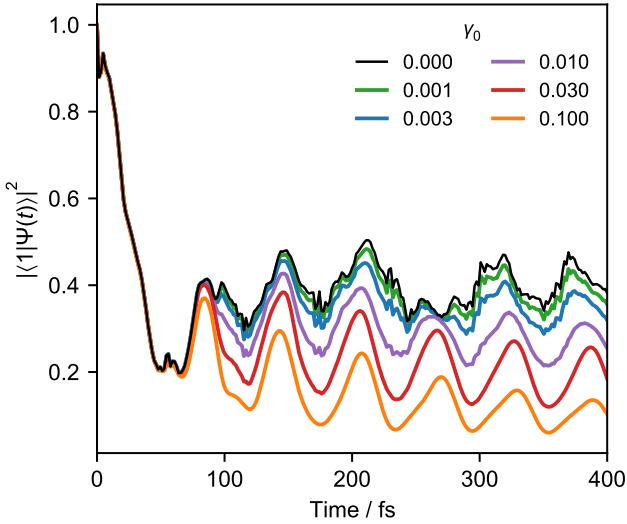


Figure 6. Populations of the pyrazine LVC Hamiltonian with different values of system-bath coupling strength γ_0 at a temperature of 300 K. As γ_0 is increased, the fine structure of the closed-system result ($\gamma_0 = 0$) are lost and the coherent oscillations gradually decrease in magnitude.

where $\mathcal{D}[\hat{L}_j]$ is the Lindblad superoperator for the jump operator \hat{L}_j .

Ordinarily, thermal dissipation is added to a VC Hamiltonian by coupling the vibrational modes to a bath of harmonic oscillators [1, 37]. A finite-temperature bath corresponds to jump operators $(\gamma_j(\bar{n}_j+1))^{1/2}\hat{a}_j$ and $(\gamma_j\bar{n}_j)^{1/2}\hat{a}_j^\dagger$ for cooling and heating of mode j , respectively [37], where γ_j is the system-bath coupling strength and Bose-Einstein coefficients $\bar{n}_j = (\exp(\omega_j/k_B T) - 1)^{-1}$ describe the occupation numbers of the bath at temperature T . These assumptions give the master equation

$$\begin{aligned} \partial\hat{\rho}/\partial t = & -i[\hat{H}, \hat{\rho}] \\ & + \sum_j \gamma_j \left((\bar{n}_j + 1)\mathcal{D}[\hat{a}_j] + \bar{n}_j\mathcal{D}[\hat{a}_j^\dagger] \right) \hat{\rho}. \end{aligned} \quad (\text{D2})$$

Ion-trap quantum computers typically require the ions to be in the ground state of the trap, which is usually achieved by laser cooling. In general, applied lasers both cool and heat; in the resolved sideband limit, the combined evolution due to laser cooling and heating of mode j takes the form [47]

$$\partial\hat{\rho}/\partial t = -i[\hat{H}, \hat{\rho}] + \sum_j A_j^- \mathcal{D}[\hat{a}_j] \hat{\rho} + A_j^+ \mathcal{D}[\hat{a}_j^\dagger] \hat{\rho}, \quad (\text{D3})$$

where A_j^- (or, for heating, A_j^+) is given by

$$A_j^\pm = \eta_j^2 \Gamma_j (B_j(\Delta \pm \omega_j^{\text{ion}}) + \alpha B_j(\Delta)), \quad (\text{D4})$$

$$B_j(\Delta) = \frac{\Omega_0^2}{\Gamma_j^2 + 4\Delta^2}, \quad (\text{D5})$$

where η_j is the Lamb-Dicke parameter, Γ_j is the spontaneous emission rate of the carrier transition, Δ is the detuning from the carrier transition, α is the angular factor for spontaneous emission ($\sim 2/5$ for dipole transitions [47]), and $\Omega_0 \ll \Gamma_j$ is the Rabi frequency of the carrier transition [47].

Comparing Eqs. D2 and D3 shows that laser cooling and heating can simulate the molecular thermal dissipation provided that the experimental parameters are chosen so that $\gamma_j = A_j^- - A_j^+$ and $\bar{n}_j = A_j^+ / (A_j^- - A_j^+)$. This can be achieved in two steps. First, because $A_j^+ / (A_j^- - A_j^+)$ depends only on Δ and Γ_j , those two parameters can be chosen to simulate a specific \bar{n}_j and, therefore, the temperature. Second, $A_j^- - A_j^+$ is proportional to the square of the remaining free parameter, the Rabi frequency Ω_0 , which depends on the tunable laser intensity and can, therefore, be used to set the system-bath interaction γ_j .

The experimental system-bath coupling strengths γ_j must be scaled to the frequencies of the simulator, as was done for \hat{H} . Such a rescaling amounts to a change of timescale in Eq. D2, giving Rabi frequencies in Hz–kHz instead of GHz–THz. By contrast, the occupation numbers \bar{n}_j are dimensionless quantities, and thus require no further scaling. The difference between typical molecular and trapped-ion frequencies results in a difference in their vibrational temperatures because the invariable \bar{n}_j depends only on $\omega_j/k_B T$. For example, a simulation at ~ 300 K corresponds to an ion-trap vibrational temperature of ~ 30 μ K, which is readily achievable in ion traps [48].

Fig. 6 shows an example of weak system-bath coupling with the LVC model of pyrazine at 300 K. The simulation assumes an Ohmic form of system-bath couplings that is widely used in chemical dynamics [37], $\gamma_j = \gamma_0 \omega_j e^{-\omega_j/\omega_0}$, where γ_0 is a constant damping parameter and ω_0 are high-frequency cutoffs.

Overall, our scheme requires at most one laser-cooling interaction per mode. However, in some chemically relevant cases, it may be possible to simulate open-system dynamics with many fewer cooling lasers. In particular, chemical dynamics often takes place at low temperatures ($k_B T \ll \omega_j$), in which case it may be possible to simultaneously cool all the vibrational modes with a broadband cooling laser. Typical frequencies of molecular vibrations are tens of THz, meaning that $\bar{n}_j \ll 1$ even at room temperature. In that limit, Eq. D2 reduces to

$$\partial\hat{\rho}/\partial t = -i[\hat{H}, \hat{\rho}] + \sum_j \gamma_j \mathcal{D}[\hat{a}_j] \hat{\rho}. \quad (\text{D6})$$

If we also assume that all the γ_j are comparable (which is true for an Ohmic spectral density and comparable ω_j), we arrive at a master equation that can be simulated with just one broadband cooling laser (e.g. using EIT cooling [49]), which can cool all the modes simultaneously. For example, repeating the simulation of Fig. 6 with a single cooling laser and equal γ_j leads to imperceptible changes in the populations shown.

E. Numerical methods

Simulations of the closed-system LVC model of pyrazine [37] were performed using NumPy [50] and SciPy [51] with the number of vibrational eigenstates truncated to 20 for both modes (ν_{6a} and ν_{10a}). Open-system dynamics used the Lindblad master-equation solver in QuTiP [52].